The Surface Circulation of the Caribbean Sea and the Gulf of Mexico as Inferred from Satellite Altimetry

AIDA ALVERA-AZCÁRATE AND ALEXANDER BARTH

Astrophysics, Geophysics and Oceanography Department, GeoHydrodynamics and Environmental Research, University of Liège, Liège, Belgium

ROBERT H. WEISBERG

College of Marine Science, University of South Florida, St. Petersburg, Florida

(Manuscript received 24 January 2007, in final form 2 September 2008)

ABSTRACT

The surface circulation of the Caribbean Sea and Gulf of Mexico is studied using 13 years of satellite altimetry data. Variability in the Caribbean Sea is evident over several time scales. At the annual scale, sea surface height (SSH) varies mainly by a seasonal steric effect. Interannually, a longer cycle affects the SSH slope across the current and hence the intensity of the Caribbean Current. This cycle is found to be related to changes in the wind intensity, the wind stress curl, and El Niño–Southern Oscillation. At shorter time scales, eddies and meanders are observed in the Caribbean Current, and their propagation speed is explained by baroclinic instabilities under the combined effect of vertical shear and the β effect. Then the Loop Current (LC) is considered, focusing on the anticyclonic eddies shed by it and the intrusion of the LC into the Gulf of Mexico through time. Twelve of the 21 anticyclonic eddies observed to detach from the LC are shed from July to September, suggesting a seasonality in the timing of these events. Also, a relation is found between the intrusion of the LC into the Gulf of Mexico and the size of the eddies shed from it: larger intrusions trigger smaller eddies. A series of extreme LC intrusions into the Gulf of Mexico, when the LC is observed as far as 92°W, are described. The analyses herein suggest that the frequency of such events has increased in recent years, with only one event occurring in 1993 versus three from 2002 to 2006. Transport through the Straits of Florida appears to decrease during these extreme intrusions.

1. Introduction

The Caribbean Sea is characterized by westward currents flowing from the Lesser Antilles to the Gulf of Mexico (GoM). These currents are fed by waters of South Atlantic origin entering through the southern Lesser Antilles as well as waters of North Atlantic origin that recirculate southwestward and enter the Caribbean through the northern Lesser Antilles (Johns et al. 2002). The major source of variability in the Caribbean Current is the propagation of meanders and anticyclonic eddies, usually called Caribbean eddies (Pratt and Maul 2000). Many studies involving surface drifters have detected the complex nature of the Caribbean Current (e.g., Molinari et al. 1981; Carton and Chao 1999; Pratt and Maul 2000; Centurioni and Niiler 2003; Richardson 2005). As the Caribbean Current arrives at the Yucatan Channel (YC), the Caribbean eddies are thought to influence the eddy-shedding events of the Loop Current (LC) (e.g., Murphy et al. 1999; Oey et al. 2003). The circulation in the GoM is characterized by the fluctuations of the LC, which irregularly sheds anticyclonic eddies that travel westward into the GoM (Leben and Born 1993; Hamilton et al. 1999). Whereas the frequency of LC eddy shedding has been studied by many authors (e.g., Maul and Vukovich 1993; Sturges 1994; Vukovich 1995; Sturges and Leben 2000; Leben 2005), the mechanisms for eddy detachment remain unknown. Small cyclonic eddies generated at irregular intervals tend to travel along the LC edge. It has been hypothesized that the small cyclonic eddies influence

Corresponding author address: Aida Alvera-Azcárate, AGO–GHER, University of Liège, Allée du 6 Août 17, Sart-Tilman, 4000 Liège, Belgium.
E-mail: a.alvera@ulg.ac.be

DOI: 10.1175/2008JPO3765.1

the shedding of the large anticyclonic LC eddies (Lee et al. 1995; Fratantoni et al. 1998; Zavala-Hidalgo et al. 2003; Schmitz 2005).

With the Caribbean Sea and the GoM characterized by complex circulation paths, many authors (e.g., Oey et al. 2003; Richardson 2005) agree that additional research is needed to better understand the flow field kinematics and dynamics. In particular, the role of Caribbean eddies in the LC eddy-shedding process remains unclear as well as the mechanisms that trigger an anticyclonic LC eddy-shedding event.

Since the launch of the Ocean Topography Experiment (TOPEX)/Poseidon and the European Remote Sensing altimetry satellites, *ERS-1* and *ERS-2*, in the early 1990s and with the addition of the *Geosat Follow-On* (*GFO*), *Jason-1*, and the *Envisat* satellites in 2000, 2001, and 2002 respectively (Robinson 2004), the measurement of mesoscale activity over the World Ocean has become possible. More than 13 years of continuous monitoring of the Caribbean Sea and GoM circulation using altimetry provides a valuable source of data to increase our knowledge of this system. Studies using thermal satellite imagery (e.g., Sturges 1994; Vukovich 1995; Fratantoni et al. 1998) are limited to winter months due to the lack of thermal contrast over the Caribbean and GoM region in summer. In addition, clouds often obscure these satellite measurements, making it difficult to track small, moving features. For this reason, satellite altimetry as used herein stands as a useful dataset for year-round monitoring of the surface mesoscale circulation in the Caribbean Sea and GoM.

Our work is organized as follows: section 2 describes the altimetry data and includes a description of the mean surface circulation. Section 3 describes the annual and interannual variability of the Caribbean Sea as well as the mesoscale circulation variability. Section 4 describes the LC anticyclonic eddy-shedding and the intrusion of the LC into the GoM. Conclusions are given in section 5.

2. Data

Sea level anomaly (SLA, computed using data from *Jason-1*, *Envisat*, *GFO*, and TOPEX/Poseidon satellites) is provided by Collecte Localisation Satellites (CLS) in France. Several corrections are applied to this dataset [inverse barometer, tides, orbit-reduction error, wet/dry troposphere; see, e.g., Le Traon and Ogor (1998); Dorandeu and Le Traon (1999)]. Along-track SLA data are low-pass filtered using a 35-km median filter and a Lanczos filter with a cutoff wavelength of 42 km (Larnicol et al. 1995). The result is gridded into a $^1/_3°$ by $^1/_3°$ resolution grid using a global optimal analysis (Le Traon et al. 1998; Ducet et al. 2000). In this work we study the period from October 1992 to February 2006 using CLS ''delayed time'' data from 1992 to January 2005 and ''near real time'' data from January 2005 to the end of the record. The delayed time dataset is of higher quality than the near real time dataset since more data are used in its computation. To obtain absolute sea surface height (SSH) we add a mean SSH obtained from the Miami Isopycnic Coordinate Ocean Model (MICOM) (Chassignet and Garraffo 2001), which has $^1/_{12}°$ resolution and was forced by European Centre for Medium-Range Weather Forecast (ECMWF) fields. The MICOM model was run for six years and the mean SSH was computed using years 4 and 5 of this simulation (see details at Chassignet and Garraffo 2001). From this absolute SSH we calculate the geostrophic currents as the gradient of SSH (with forward differences in the edges of the SSH matrix and centered differences at the interior points). The east and north components, u and v, of the geostrophic velocity vectors are calculated by

$$u = -\frac{g}{fR}\frac{\partial\zeta}{\partial\lambda}; \quad v = \frac{g}{f}\frac{1}{R\cos(\lambda)}\frac{\partial\zeta}{\partial\phi}, \tag{1}$$

where λ is the latitude, ϕ the longitude, R the earth's radius, ζ the elevation, f the Coriolis parameter, and g the acceleration due to gravity.

Description of the mean geostrophic currents field

Figure 1a presents the bathymetry of the Caribbean Sea, the GoM, and the U.S. southeast coast. Superimposed on the bathymetry is the mean geostrophic current field. Figure 1b shows the instantaneous SSH field and the corresponding geostrophic currents, sampled on 13 October 2004, to illustrate the spatial variability that is characteristic of this region. For example, the Caribbean Current mean direction is westward (Fig. 1a), but it describes (Fig. 1b) large meanders from the Lesser Antilles to the Nicaraguan Rise (see geographic names in Fig. 2).

For comparison with previous studies, the maximum geostrophic currents, Eq. (1), sampled in the Caribbean Sea box of Fig. 1 can be as high as 1.28 m s^{-1}. The average of the highest velocity measured at each time step within the same domain is 0.82 m s^{-1} (with a standard deviation of 0.14 m s^{-1}). Centurioni and Niiler (2003), Hernández-Guerra and Joyce (2000), Fratantoni (2001), and Molinari et al. (1981) found similar maximum speeds for the Caribbean Current.

The bathymetry plays a key role in the mean circulation of the Caribbean Sea. Two major flow features are observed in the figure: the Panama–Colombia cyclonic gyre (Richardson 2005) and the steering of the Caribbean Current by the Nicaraguan Rise. The Panama–Colombia cyclonic gyre is a permanent feature of the

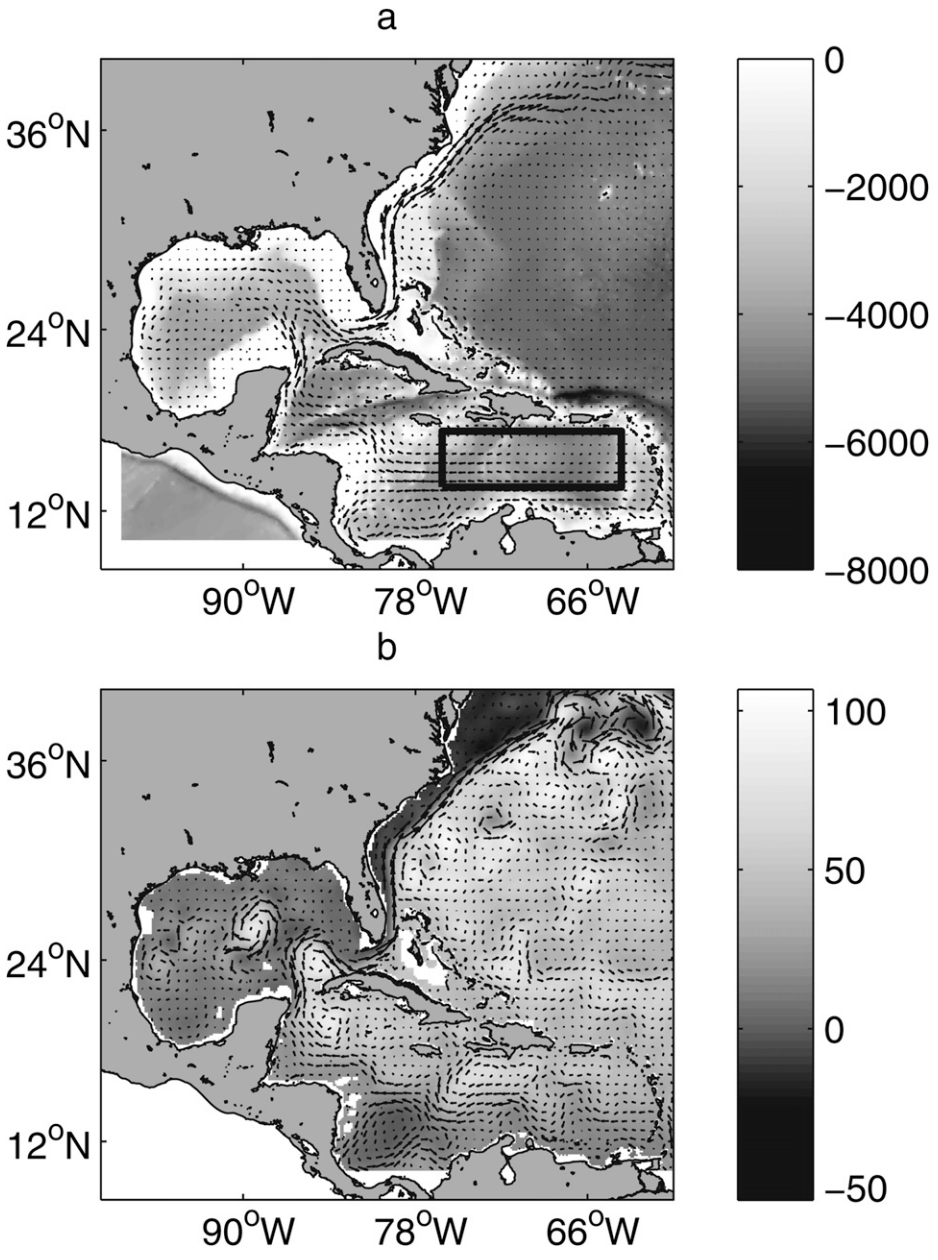

FIG. 1. (a) Bathymetry (m) of the Caribbean Sea, Gulf of Mexico, and U.S. southeast coast: Superimposed are the mean geostrophic currents. (b) Example of an instantaneous SSH field and geostrophic currents on 13 Oct 2004.

Panama–Colombia Basin. The steering by the Nicaraguan Rise causes the Caribbean Current to first turn sharply north before returning west to form a western boundary current along the Mexico coast.

When passing through the YC, the Campeche Bank also influences the direction taken by the LC as it enters the GoM. Once in the GoM, we observe two modes in the LC intrusion. The first mode, with the LC reaching about 24°N, represents the most common LC intrusion into the GoM, as in Fig. 1b. The second mode, reaching about 28°N, represents the larger LC intrusions. These LC intrusions will be discussed in section 4.

3. Caribbean Current and Caribbean eddies

a. Interannual cycle

The frequency and speed of the Caribbean eddies and meanders is tracked along the mean SSH 35-cm isoline,

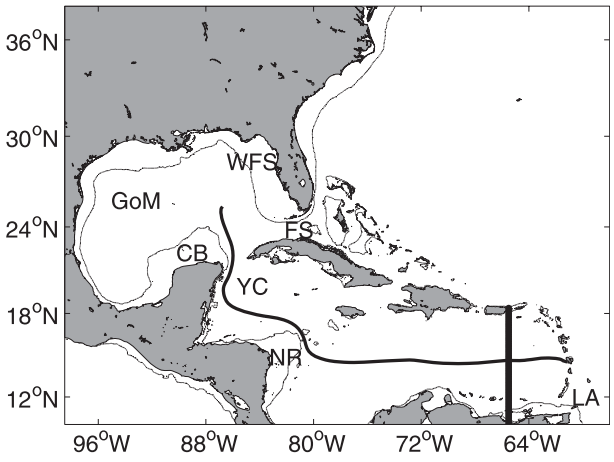

FIG. 2. Path used to calculate the Hovmöller diagram of Fig. 3 (bold line). Also included is a north–south transect in the Caribbean Sea at 65.5°W. The thin line marks the 200-m isobath. Geographic regions are the Lesser Antilles (LA), Nicaraguan Rise (NR), Yucatan Channel (YC), Campeche Bank (CB), Gulf of Mexico (GoM), and the West Florida shelf (WFS).

which closely follows the path of the Caribbean Current (Fig. 2). The Hovmöller diagram of Fig. 3 shows the evolution of the SLA along this isoline from October 1992 to February 2006.

The most prominent feature of the Caribbean Sea SSH variability is the westward propagation of eddies and meanders (Fig. 3). The characteristics of these features will be addressed in section 3b. Focusing on the annual to interannual variability, we notice an annual cycle of positive and negative SLA over the eastern Caribbean Sea (between 0 and 500 km in Fig. 3). The SLA is negative each year from January to May, followed by a positive period. This annual cycle is driven by the steric response of the Caribbean Sea to cooling and heating fluxes at the surface.

The Fourier spectrum of the Caribbean Sea SSH variability is presented in Fig. 4. A total of $N = 1658$ time series (each one corresponding to a spatial point in the Caribbean Sea and with a length of $m = 709$ temporal data points) were used to compute the spectrum. However, not all spatial points are independent, as there is a nonnegligible spatial correlation. To estimate the effective number of degrees of freedom from the 1658 spatial points, we used a technique, proposed by Bretherton et al. (1999), based on the partitioning of variance between the empirical orthogonal functions calculated from the dataset

$$N^* = \left(\sum_{k=1}^{N} \mu_k\right)^2 \Big/ \sum_{k=1}^{N} \mu_k^2, \qquad (2)$$

with μ the eigenvalues of the dataset. The effective number of degrees of freedom for our dataset, calculated using Eq. (2), is $N^* = 37$. A 95% significance line is included in the figure, calculated using a Fisher–Snedecor F distribution with $2N^*$ and $2(m - 1)N^*$ degrees of freedom, following Fuller (1996). For a large number of time steps (m), the F distribution converges toward a χ^2 distribution. In our case the significance level would be essentially the same for a χ^2 distribution with $2N^*$ degrees of freedom.

The annual time scale is the most energetic feature in the spectrum of Fig. 4, accounting for about 10.8% of the total energy, although energy is also contained in higher harmonics, that is, at 6 and 3 months with 3% and 3.7% of the total energy, respectively. If we integrate the energy contained from 3 to 6 months, then up to 23% of the total energy is contained in this time range. These short time-scale variations are due in part to the propagation of cyclonic and anticyclonic eddies through the Caribbean Sea and will be addressed in the next subsection. At interannual time scales, a peak is detected at a frequency of about 4 yr. This peak contains about 2.7% of the total variance, which is still considerable since most of the energy is contained at time scales from 3 months to a year.

To further investigate the annual cycle and the peak detected at around four years in Fig. 4, a complex empirical orthogonal function (CEOF) analysis is used to determine the structure of the annual and interannual variability of the Caribbean Sea. The SSH data are first bandpass filtered to retain the desired frequency range (e.g., periodicities from 330 to 385 days are retained to study the annual variability). Then the Hilbert transform is calculated to retain phase information, and the CEOFs are obtained from the Hilbert transformed data. Figure 5 shows the spatial maps of amplitude and phase for the first CEOF mode at the annual frequency. The phase of the first mode is spatially uniform over the entire Caribbean basin, representing the annual steric variation in the SSH. The amplitude is largest in the eastern Caribbean basin, and with the first CEOF mode accounting for 97.1% of the total variability, the steric variation dominates the annual cycle of SSH in the Caribbean. The annual cycle reaches its maximum in October, coincident with the end of the summer season in the Caribbean Sea.

A similar analysis is carried out at the frequency peak centered at around 4 yr. The first CEOF retains 68% of the variability, and the spatial maps of amplitude and phase of this CEOF are presented in Fig. 6. The phase distribution shows a clear oscillation of the Caribbean SSH, with a nodal line along the path of the Caribbean Current. The amplitude map indicates that this oscillation

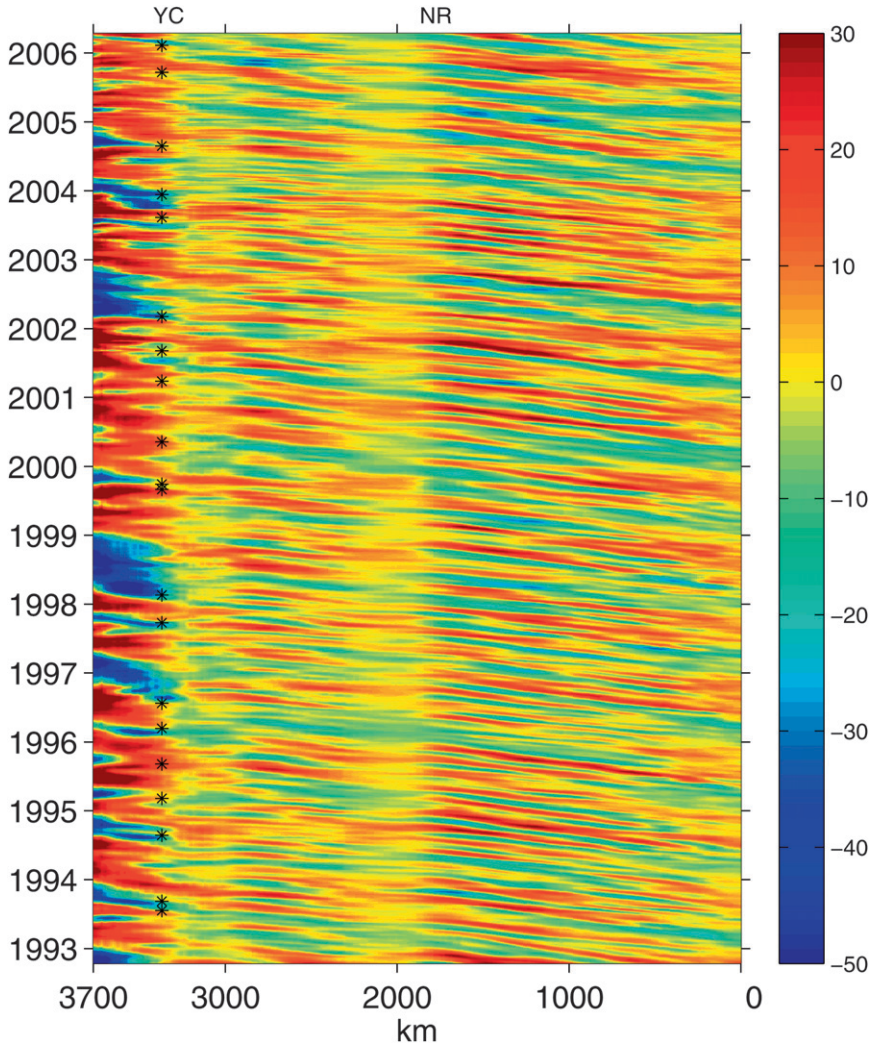

FIG. 3. Hovmöller diagram of the sea surface height anomaly along the path shown in Fig. 2. The origin (0 km) is located in the Lesser Antilles and the Yucatan Channel is located at 3500 km. The approximate location of the Yucatan Channel (YC) and the Nicaraguan Rise (NR) is indicated. Year labels correspond to 1 Jan of each year. Asterisks, located at the YC, mark the date of an eddy shedding. The location of the asterisks in space does not reflect the actual position of the eddy detachment.

is largest at the northern and southern limits of the Caribbean Sea. This finding indicates a change in the north–south slope of the Caribbean Current, with an approximate period of 4 yr. A change in the slope corresponds to a change of the Caribbean Current surface velocity and presumably also its transport.

The 4-yr cycle in the westward Caribbean Current transport appears to be highly correlated to changes in the westward component of the wind field. Monthly winds from the International Comprehensive Ocean–Atmosphere Data Set (ICOADS) (Worley et al. 2005) over the Caribbean Sea are used for the period covered by the altimetry dataset. In Fig. 7 the spatially averaged zonal winds with a 12-month low-pass filter are represented as well as the unfiltered winds. The averaged winds are consistently directed to the west. Also in the figure is a time series of the SSH difference between two points in the Caribbean Sea (to the north and to the south of the Caribbean Current main axis; see Fig. 2), which is used as a proxy of the intensity of the Caribbean Current. The SSH north − south difference time series is averaged at the monthly time step of the wind field and a 12-month low-pass filter is applied. The correlation between the filtered winds and the filtered SSH north − south difference in the Caribbean is −0.6 (significant at the 99% level), with stronger winds toward

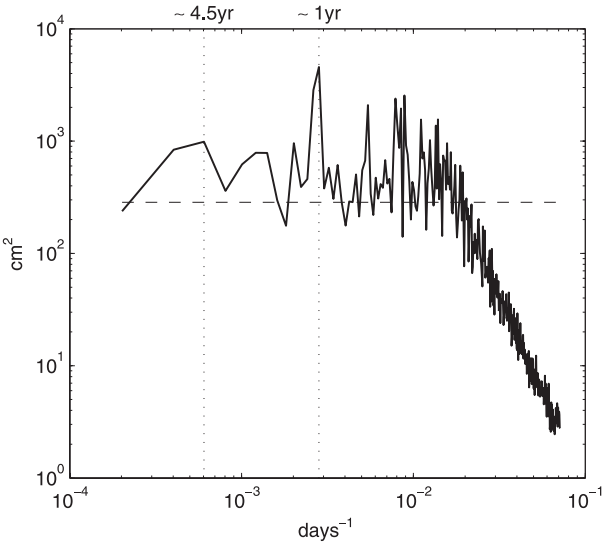

FIG. 4. Fourier transform of the SSH over the Caribbean Sea. The dotted lines show the frequency at about 1 and 4 yr. The dashed line shows the 95% significance level.

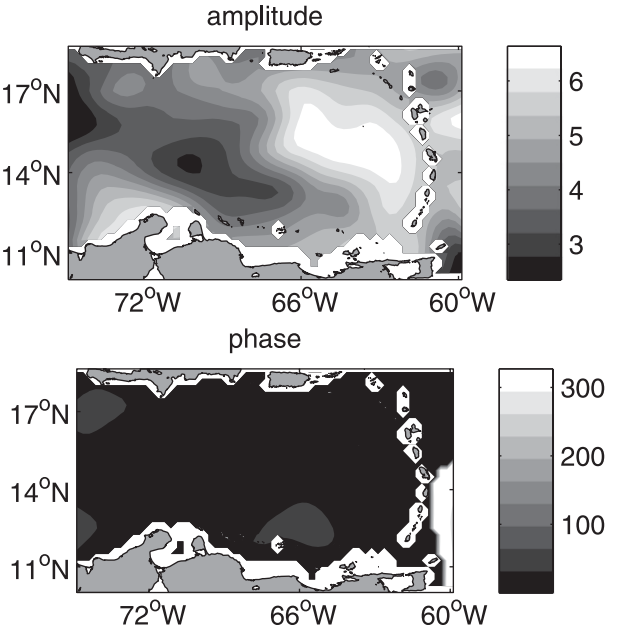

FIG. 5. Amplitude (cm) and phase (deg) of the first CEOF centered at 1-yr frequency.

the west corresponding to a larger north − south difference in the Caribbean SSH and, therefore, to an increased transport of the Caribbean Current. The annual cycle is not included in the correlation since it has been removed by the low-pass filter.

The curl associated with the wind stress field in the Caribbean Sea is consistently positive south of the Caribbean Current main axis position (about 14°N) and negative north of that position. The 12-month low-pass filtered wind stress curl does also exhibit an interannual cycle at the same frequency as the SSH north − south difference at all latitudes in the Caribbean Sea (data not shown). Stronger easterly winds bring positive anomalies to the southern Caribbean and negative curl anomalies to the northern Caribbean. This might induce a stronger upwelling in the southern Caribbean, which would result in a lowering of the steric height in that zone, and a stronger downwelling in the northern Caribbean, resulting in a rising of the steric height there. The combination of these two effects might explain the observed changes in the slope of the Caribbean Sea. The strongest correlation between the SSH north − south difference and the wind stress curl (−0.56, significant at the 99% level) is found at 14.5°N, with strong (negative) curl corresponding to a larger north–south slope of the Caribbean Current. In the southern part of the Caribbean Sea, the highest correlation (0.37, significant at the 99% level) is found at 11.5°N.

Finally, the correlation between the SSH slope and the El Niño–Southern Oscillation index [Wolter (1987) with a 12-month low-pass filter, data not shown] is 0.7, significant at the 99% level. This indicates that the observed 4-yr cycle in the Caribbean Sea may be related to variations recurring over larger spatial scales.

The average north − south SSH difference for the Caribbean Current is about 0.4 m (Fig. 7). Considering a north–south transect of 4° latitude, the geostrophic current associated with that slope is -0.28 m s^{-1}, which integrated over a surface layer of 200 m [the typical depth of the Caribbean Current, e.g., Morrison and Smith (1990)] translates to a total transport of 22.4 Sv (1 Sv $\equiv 10^6$ m^3 s^{-1}). This transport is in agreement to what has been observed in the eastern Caribbean Sea (Johns et al. 2002). A variation of 0.05 m of the Caribbean Current north − south difference (the typical amplitude variation of the 4-yr cycle observed in Fig. 7) would then be associated with a change in transport of about 2.8 Sv, that is, about 12.5% of the total transport.

Similar analyses of the SSH record indicate that the 4-yr cycle is present along the path of the Caribbean Current. Analyses of the transport through the Straits of Florida (SF), as measured by a submarine cable at 27°N (Baringer and Larsen 2001), show some energy at the 4-yr frequency band (not shown), although it does not show a significant correlation with the cycle present in the Caribbean Sea.

A further manifestation of interannual variability in the Caribbean Sea are anomalous seasons, such as occurred in winter 2003. The negative SLA period was very weak that year (see the SLA on Fig. 3), causing the winter 2003 SLA to resemble the summer SLA. This

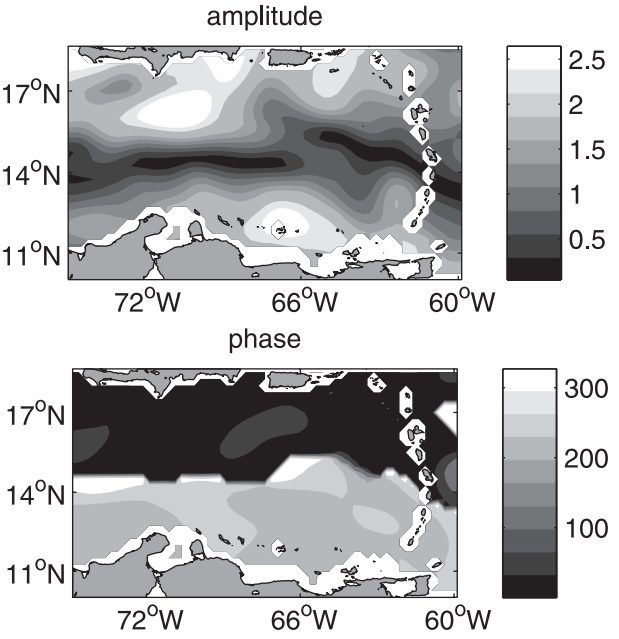

FIG. 6. As in Fig. 5, but at 4-yr frequency.

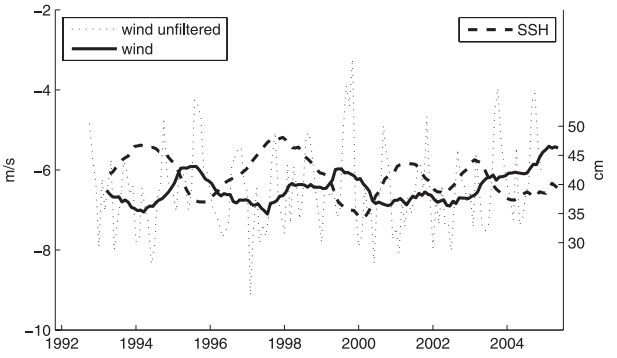

FIG. 7. Monthly winds and SSH north − south difference over the Caribbean Sea. Both datasets have been filtered with a 12-month low-pass filter. The unfiltered winds are also included.

may have resulted from interannual variations in the intertropical convergence zone (ITCZ) position. In a normal year, the ITCZ moves southward in winter when the Caribbean Sea SLA becomes negative. In summer, the ITCZ moves northward when the SLA over the Caribbean is positive. In 2003 the ITCZ was anomalously positioned to the north (e.g., Cassou et al. 2005), causing summerlike conditions to the Caribbean Sea during winter. This northern ITCZ position brought wet conditions to the Caribbean, favoring the European heat wave in summer 2003 (Schär et al. 2004; Cassou et al. 2005). Global temperatures in 2003 were 0.5°C warmer than the long-term mean, affecting also the Caribbean Sea (Levinson and Waple 2004). In addition, from January to April 2003 the effects of the 2002 El Niño episode were still present. All of these conditions may have influenced the anomalous Caribbean SLA values in winter 2003.

To summarize, the Caribbean Sea SSH is affected by the annual cycle, which mainly consists of a steric variation (i.e., the homogeneous response of the SSH to the heating/cooling fluxes at the surface), plus interannual variations (about a 4-yr cycle) of the north–south slope of the Caribbean Current that, therefore, affects its geostrophic transport. Isolated events, such as the anomalous winter of 2003, are also observed, but the time series is too short to infer conclusions about their periodicity.

b. Caribbean eddies and meanders

The Hovmöller diagram of Fig. 3 shows a regular occurrence of Caribbean eddies and meanders traveling westward from the Lesser Antilles to the Nicaraguan Rise. There are 56 Caribbean eddies and meanders observed from the Lesser Antilles to the Nicaraguan Rise. This corresponds to about 4.3 eddies per year, slightly lower than the estimation by Pratt and Maul (2000) from 1992 to 1995 (about 4.6 events per year). Considering only a zone in the Hovmöller diagram when the flow of eddies is more or less constant, then 5.7 eddies per year are observed. These numbers are higher than the number of eddies typically detached from the LC in the GoM each year (Vukovich 1995; Sturges 1994; Sturges and Leben 2000), corresponding to a ratio of approximately three Caribbean features for each LC eddy.

Three distinct zones are observed in Fig. 3. These zones, corresponding to the Venezuela–Colombia Basin, the Cayman Basin (between the Nicaraguan Rise and the YC), and the GoM, present different characteristics. Although at the Venezuela–Colombia Basin the propagating features are well defined and present a near-regular frequency, these features become less defined in the Cayman Basin and their speed of propagation increases compared to the Venezuela–Colombia Basin. Some of them disappear after passing the Nicaraguan Rise, in agreement with observations based on surface drifters (e.g., Richardson 2005). The interaction with the shallow bathymetry and the change in direction of the main current cause the decrease in intensity of the Caribbean eddies and meanders in this zone. The propagation speed of these features can be calculated by the Radon method (e.g., Challenor et al. 2001). The Radon transform projects the Hovmöller diagram into a rotated coordinate system. The angle that maximizes the square of the sum of the projection gives the propagation speed of the studied feature. If we calculate the propagation speed separately for each basin, we obtain 0.11 ± 0.04 m s^{-1} for the Venezuela–Colombia Basin and 0.13 ± 0.08 m s^{-1} for the Cayman Basin (see the

appendix for a description on the Radon transform and how the standard deviation is obtained). These estimates are in agreement with other studies (Carton and Chao 1999; Murphy et al. 1999; Richardson 2005). The speeds in both basins appear not to be significantly different. The third zone in Fig. 3, the GoM, will be discussed in more detail in section 4.

The features propagating in the Caribbean Sea are considered as eddies by some authors (e.g., Carton and Chao 1999; Murphy et al. 1999; Richardson 2005), whereas other authors (e.g., Molinari et al. 1981; Pratt and Maul 2000) mention the possibility that these features are actually meanders rather than closed eddies. Furthermore, the Caribbean eddies are thought to originate from the North Brazil Current retroflection eddies that pass the Lesser Antilles and enter the Caribbean Sea. As observed by Goni and Johns (2001), the number of eddies entering the Caribbean Sea through the southern Lesser Antilles could be as low as one per year, clearly different to the number of propagating features in the Hovmöller diagram.

To understand the dynamics of the Caribbean eddies and meanders, and in particular to determine which factors influence the propagation speed of the Caribbean features, we used the idealized Phillips model for two-layered flows (Phillips 1954; Pedlosky 1979). We consider that the flow in the Caribbean Sea is formed by two layers, with a pure zonal velocity U_n (westward in our case), where $n = 1$ refers to the surface layer and $n = 2$ to the bottom layer. The Phillips model assumes that U_1 and U_2 are independent of latitude and longitude. If the speed of both layers is different, $U_1 \neq U_2$, geostrophy implies that there is a slope at the interface between these two layers. This slope acts as a source of potential energy that allows disturbances to grow. A perturbation in a two-layer, quasigeostrophic fluid on a β plane propagates with two possible phase speeds:

$$c_{a,b} = U_2 + \frac{U_s K^2 (K^2 + 2F_2) - \beta(2K^2 + F_1 + F_2)}{2K^2(K^2 + F_1 + F_2)} \pm \frac{[\beta^2 (F_1 + F_2)^2 + 2\beta U_s K^4 (F_1 - F_2) - K^4 U_s^2 (4F_1F_2 - K^4)]^{1/2}}{2K^2(K^2 + F_1 + F_2)}, \quad (3)$$

where $U_s = U_1 - U_2$, $\beta = 2.22 \times 10^{-11}\text{m}^{-1}\text{s}^{-1}$, and K is the total wavenumber of the perturbation; $F_n = f^2/g'D_n$ with the Coriolis frequency $f = 3.76 \times 10^{-5}\ \text{s}^{-1}$; $g' = g(\rho_2 - \rho_1)/\rho_0 = 0.0172\ \text{m s}^{-2}$, the reduced gravity; and D_n the thickness of layer n. We want to assess, through a sensitivity study, the importance of two key parameters: the velocity of the surface layer and the wavenumber of the propagating features. The values of the parameters needed to diagnose Eq. (3) are derived either from the altimetry dataset or, if this is not possible, from the Naval Research Laboratory Atlantic Hybrid Coordinate Ocean Model (HYCOM) (Chassignet et al. 2007). HYCOM is the follow-up version of the MICOM model and uses the mean SSH calculated from MICOM (Chassignet et al. 2007), so the use of HYCOM for the parameter choice in this section stands as the more suitable option.

The surface and bottom layers are considered to be 200 m (Morrison and Smith 1990; Carton and Chao 1999) and 4000 m thick, respectively. The average speed of the bottom layer is taken to be $-0.001\ \text{m s}^{-1}$, a value obtained from HYCOM. The surface layer mean velocity is $-0.17\ \text{m s}^{-1}$, as obtained through the geostrophic analysis of the SSH dataset. The mean velocity over the upper 200 m of the water column in HYCOM (using model results from 2004 and 2005) is $-0.22\ \text{m s}^{-1}$ with a standard deviation of $0.04\ \text{m s}^{-1}$. Thus, the surface layer velocity is considered to vary between -0.17 and $-0.26\ \text{m s}^{-1}$.

For the zonal wavenumber (k_x), we use the speed of propagation of the Caribbean features ($0.11\ \text{m s}^{-1}$) obtained by the Radon method and the estimate of 5.7 eddies per year made previously in this section. This corresponds to a zonal wavelength of 550 km, and we consider an interval of $\pm$ 100 km to account for the uncertainty of this parameter. For the meridional wavenumber (k_y), the fundamental mode in the north–south direction was chosen, based on the spatial structure of the altimetry data, which shows a crest on the middle of the basin and nodes at the north and south edges. The meridional extension of the basin is about $L = 600$ km, and the associated wavenumber is $k_y = \pi/L$.

The total wavenumber $K = \sqrt{k_x^2 + k_y^2}$ then varies from 0.015 to 0.01 km^{-1}, or from 420 to 575 km if we consider the total wavelength $2\pi/K$.

Equation (3), which takes the vertical shear and the β effect into account, contains solutions for Rossby waves and baroclinic instabilities as special cases. The Phillips model does not include, however, the existence of barotropic instabilities within the domain since the horizontal velocity shear is not taken into account. To establish the importance of the available energy for baroclinic and barotropic instabilities in the Caribbean Sea, and following Killworth (1980), we computed the ratio between the front length scale and the internal deformation radius. Considering an internal deformation radius of 60–80 km (Chelton et al. 1998) and a front length scale of 300–500 km, this parameter is about 4–8. Killworth (1980) showed that, if $\lambda \gg 1$ (i.e., the horizontal length scale is much larger than the deformation radius), the process that dominates the transfer of energy between the mean flow and the perturbations is through baroclinic instability. Based on this simple analysis, the baroclinic processes in the Caribbean are expected to be larger than the barotropic processes, but there is not an order of magnitude in this difference.

The relative importance of the barotropic and baroclinic processes can also be obtained by examining the kinetic and available potential energy transfer from the mean flow to the perturbations. We calculated the barotropic and baroclinic energy conversion terms for the Caribbean Sea (following Hart 1974; Killworth 1980; Kontoyiannis 1997; Qiao and Weisberg 1998) using data from the HYCOM model. We consider the variables u (east–west velocity), v (north–south velocity), and ρ (density) as the sum of an average field and a perturbation field according to the Reynolds decomposition:

$$u = \bar{u} + u', \tag{4}$$

$$v = \bar{v} + v', \tag{5}$$

and

$$\rho = \bar{\rho} + \rho'. \tag{6}$$

Primes denote deviation of a variable with respect to a suitably chosen mean, specified with an overbar. The averages are calculated using a FFT filter with a 2-month window. Two months were chosen as a typical time scale for an eddy to traverse a given point in the Caribbean Sea from east to west.

The transfer of kinetic energy from the mean flow contributes to the growth of barotropic instabilities. For a westward flow, with the velocity varying only with latitude, the transfer of kinetic energy (TKE) is given by

$$\mathrm{TKE} = -\rho_0 \overline{u'v'} \bar{u}_y, \tag{7}$$

where ρ_0 is the reference density, the subscript denotes partial differentiation, and y the latitudinal coordinate. The transfer of available potential energy (TAPE) is related to barolinic instabilities and can be computed by

$$\mathrm{TAPE} = \frac{g\bar{\rho}_y \overline{\rho' v'}}{\bar{\rho}_z}, \tag{8}$$

where g is the acceleration due to gravity. All variables were calculated from the HYCOM global analysis fields, spanning 5 years. The terms TKE and TAPE are averaged over time and integrated over depth:

$$\mathrm{TKE}_{\mathrm{av}} = \frac{1}{T}\int_{t_0}^{t_1}\int_{-H}^{0} \mathrm{TKE}\, dt\, dz \tag{9}$$

and

$$\mathrm{TAPE}_{\mathrm{av}} = \frac{1}{T}\int_{t_0}^{t_1}\int_{-H}^{0} \mathrm{TAPE}\, dt\, dz, \tag{10}$$

where $T = t_0 . . . t_1$ is the total time of integration and H is the depth of the domain. From $\mathrm{TKE}_{\mathrm{av}}$ and $\mathrm{TAPE}_{\mathrm{av}}$ we can calculate the ratio between the total kinetic energy transfer and the total available potential energy transfer terms integrated over the Caribbean domain:

$$\mathrm{ratio} = \frac{\int_S \mathrm{TAPE}_{\mathrm{av}} dS}{\int_S \mathrm{TKE}_{\mathrm{av}} dS}. \tag{11}$$

The ratio between these two terms is ~5, indicating that the energy transfer in the domain is predominantly baroclinic. Both the total baroclinic and barotropic energy conversion terms are positive; therefore, the transfer of energy is from the mean flow to the perturbations, allowing these to grow. From these results we can state that, although the available energy for barotropic conversion is not neglibible, it is smaller than the available energy for baroclinic conversion, so the Phillips model can be applied. Then we will use the Phillips model to analyze the propagation speed of the Caribbean Sea disturbances. We differentiate three cases:

- *Case I: The general case.* The phase speed contains the β effect and the effect of tilted isopycnals (U_s), as described in Eq. (3). The propagation speeds and growth rate for the range of wavelengths considered are shown in Figs. 8a,b. Perturbances with wavelengths in the range 370–500 km (and up to 580 km or the faster mean upper flow) are unstable, with a

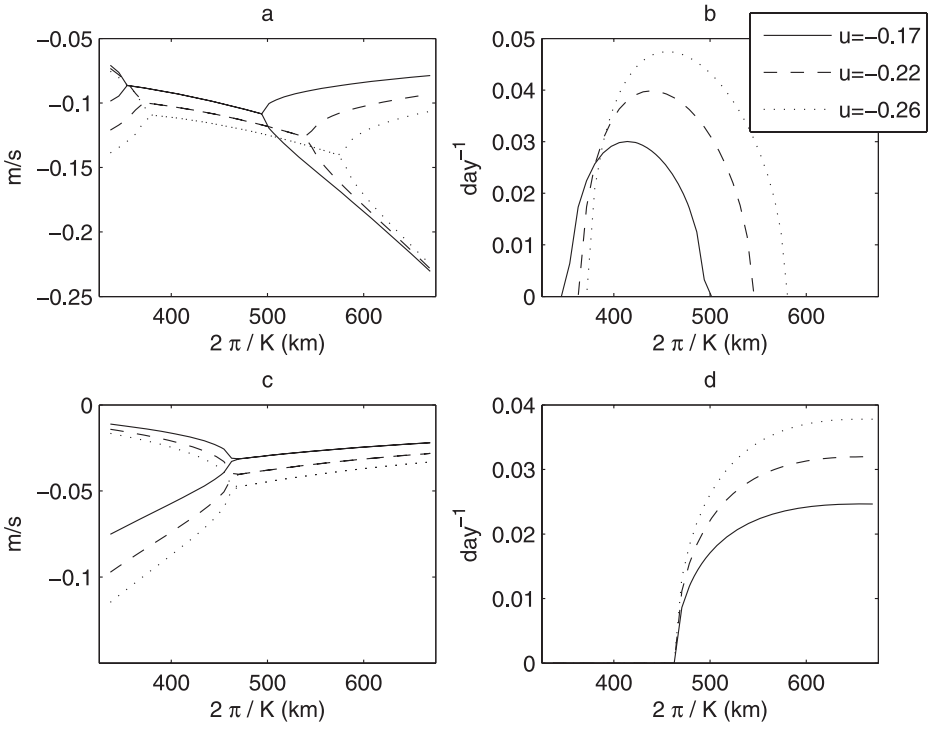

FIG. 8. Propagation speed and growth rate obtained with the Phillips model. (a),(c) Propagation speed and (b),(d) growth rate obtained when (top) both the β effect and the vertical shear are taken into account (case I) and (bottom) no β effect is included in the model (case III).

propagation speed of about -0.1 m s^{-1} and maximum growth rates of about 20–30 days [i.e., a perturbance in the Caribbean would take 20–30 days to increase its amplitude by a factor of 2.71 (i.e., the *e*-folding time)], which is too high for what is observed in the Caribbean Sea. The propagation speed of these unstable waves agrees with the observed propagation speed calculated from the Hovmöller diagram ($c = -0.1$ m s^{-1} for the Venezuela–Colombia Basin). Given the approximations of the Phillips model and the uncertainties associated with choosing parameters, these results indicate that the propagation speed of the Caribbean features is certainly consistent with expectations based on simple baroclinic instability theory.

The application of Eq. (3) provides the phase speed for perturbations under the β effect and under the effect of sloping isopycnals. However, it does not give an appreciation of the relative importance of both effects. For the purpose of discussion, we also examine the cases in which $\beta = 0$ and $U_s = 0$ to determine the phase speed of the perturbations under these simplified conditions.

- *Case II: $U_s = 0$.* The velocity is considered to be equal to the depth-averaged velocity $U = (D_1U_1 + D_2U_2)/(D_1 + D_2)$. Equation (3) is reduced to

$$c_a = U - \frac{\beta}{K^2} \tag{12}$$

and

$$c_b = U - \frac{\beta}{K^2 + F_1 + F_2}. \tag{13}$$

These solutions represent the dispersion relation for the barotropic and baroclinic Rossby waves, respectively, in the presence of the background flow U. The solutions for the propagation speed in the absence of shear are stable for all wavelengths (results not shown). The wave speeds of the two solutions do not agree with the observations: barotropic waves ($c_a \simeq -0.18$ m s^{-1}) are too fast and baroclinic Rossby waves ($c_b \simeq -0.05$ m s^{-1}) are too slow compared to the observations.

- *Case III: No β effect ($\beta = 0$) but considering the vertical shear* ($U_1 \neq U_2$). The Phillips model describes the baroclinic instability of the mean flow. The propagation speeds and growth rate are shown in Figs. 8c,d. For wavelengths around 500 km, the propagation speed is imaginary, and the two solutions correspond to exponentially growing and decaying waves, respec-

tively (in Fig. 8 only the growth rate of the growing wave is included, the decaying wave growth rate being of equal magnitude but with opposite sign). Although the range of unstable wavelengths in Fig. 8 includes the observed wavelengths of the Caribbean Current meanders and eddies, the propagation speeds are too small compared with the observations. The maximum growth rates also occur at longer wavelengths than observed. At wavelengths smaller than 400 km we find an acceptable value for the propagation speed on the lower branch of the curves, but these waves are stable and shorter than observed in the Hovmöller diagram. Therefore, the propagation speed of the Caribbean eddies cannot be explained if the β effect is not taken into account. The β effect stabilizes the flow at long wavelengths and results in higher and more realistic propagation speeds.

In conclusion, the propagation speed of the features observed in the Venezuela–Colombia Basin can be explained by baroclinic instabilities under the combined influence of vertical shear and the β effect. The SSH dataset allows one to analyze the spatial structure of these propagating features, which reveals that not all features can be clearly identified as closed-circulation anticyclonic eddies: some of the features appear to be meanders, rather than eddies, originated at the passage of the Caribbean Current through the Lesser Antilles.

4. The Loop Current and the Gulf of Mexico

The Hovmöller diagram of Fig. 3 also includes part of the GoM, where the main feature that can be observed is the intrusion of the LC into the gulf. There are intervals when the LC is positioned to the south for long periods of time, as in 1997, 1998, and 2002. During these intervals, the LC neither penetrates far into the GoM nor sheds an anticyclonic eddy. It might, however, impact the West Florida shelf if the LC interacts with the zone of isobath convergence near the Dry Tortugas (Hetland et al. 1999). This sets currents in motion over a major portion of the West Florida shelf, facilitating large upwelling and anomalous water property distributions (Weisberg and He 2003). The occurrence of these events causes major perturbations in the shelf circulation and ecology (Walsh et al. 2003; Weisberg and He 2003).

The eddy detachment events observed during the study period are also included in Fig. 3. A list of eddy detachment dates is given in Table 1. There is good agreement between the detachment of an eddy and a negative SLA in the GoM. The southward retreat of the LC after an eddy is shed is also visible in Fig. 3 (for some the LC retreats totally, for others the LC only retreats halfway back through the GoM). For a complete examination of the LC characteristics and the effect of the eddy shedding events, the Hovmöller diagram is insufficient, as some of these events happen outside the line chosen for the diagram.

a. Loop Current eddy-shedding characteristics

A total of 21 anticyclonic eddies of various sizes (from ~100 to ~300 km in diameter) were shed from the LC from October 1992 to February 2006 (Table 1). The eddies formed between the end of 1993 and 1999 are in agreement with the findings of Sturges and Leben (2000), although in our estimates the shedding dates are consistently sooner than theirs. The differences between the mean SSH used in both works and the criteria used to determine when an eddy has shed are the main causes for this mismatch. We determined visually (i.e., in a qualitative way), based on SSH and geostrophic currents, when the LC circulation is interrupted, and there are clearly two circulation cells: one forms the LC itself, flowing from the YC to the SF and the other describes a closed anticyclonic circulation within the LC eddy. When this separation occurs without future reattachment, we describe it as a successful eddy shedding. The uncertainty of the exact moment when an eddy is detached from the LC is high—up to four weeks as defined by Sturges and Leben (2000)—and the mentioned differences are usually within this uncertainty limit.

Twelve out of the 21 eddies were shed in the 3-month interval from July to September, which may indicate that a seasonal cycle influences the likelihood of a shedding event. Vukovich (1995), describing eddy-shedding events from 1972 to 1993, observed eddies at all months except December, with the peak eddy shedding in spring or summer. The shortness of our dataset does not allow us to establish if the difference between our work and the Vukovich (1995) results is due to a large-scale cycle or a switch in the behavior of the LC eddy-shedding events.

The average period between LC anticyclonic eddy separations in our dataset is 8.2 months. Most authors prefer to establish the most frequent period between eddy separations. The eddy-shedding periods of Table 1 are represented in Fig. 9 as the number of eddies shed at each period. Four eddies detached after a period of 6–7 months, the highest peak in the figure. The significance of the other peaks is difficult to determine, given the small number of eddies used. Several authors have studied the LC eddy-shedding period, with results varying depending on the dataset used, the technique to establish the significance of the shedding periods, and the criteria used to determine an eddy detachment. For example, Vukovich (1995) estimated the average shedding interval in 11 months; Maul and Vukovich (1993)

TABLE 1. Dates of Loop Current eddy detachment events, period that followed until the next eddy detachment, and dates of extreme LC intrusions.

Eddy number	Date	Period (months)	Extreme intrusion	Description
			23 Jun to 14 Jul 1993	LC up to 92°W
1	21 Jul 1993	1.63		
2	8 Sep 1993	11.67		
3	24 Aug 1994	6.53		
4	8 Mar 1995	6.07		
5	6 Sep 1995	6.3		
6	13 Mar 1996	4.43		
7	24 Jul 1996	14.23		
8	24 Sep 1997	4.9		
9	18 Feb 1998	18.67		
			21 Jul to 22 Sep 1999	LC up to 27°N
10	1 Sep 1999	0.9		
11	29 Sep 1999	7.47		
12	10 May 2000	10.73		
			21 Feb to 21 Mar 2001	LC up to 27°N
13	28 Mar 2001	5.37		
14	5 Sep 2001	6.07		
			9 Jan to 20 Feb 2002	LC up to 92°W
15	6 Mar 2002	0		
16	6 Mar 2002	17.47		
			16 Apr to 21 May 2003	LC up to 27°N
17	13 Aug 2003	4		
18	13 Dec 2003	11.1		
			31 Jul to 18 Aug 2004	LC up to 27°N
19	25 Aug 2004	13.07		
			27 Apr to 18 Jun 2005	LC up to 27°N
			3 to 14 Sep 2005	LC up to 92°W
20	21 Sep 2005	4.77		
			7 Jan to 1 Feb 2006	LC up to 92°W
21	11 Feb 2006	0.8		

found a primary peak at 12 months and secondary peaks at 8 and 6 months; Sturges (1994) found primary modes at 8–9 months and 13–14 months; and Sturges and Leben (2000) found primary modes at 6 and 11 months and a secondary mode at 9 months, a result also confirmed by Leben (2005). A consensus about the primary eddy-shedding interval remains elusive.

Also included in Fig. 9 is the size of the shed eddies, with an estimate of the mean shedding periods and the standard error of this mean. A tendency is observed where larger eddies are followed by longer periods without eddy shedding, and vice versa. The larger the size of the eddy, the larger the volume lost by the LC. After a large eddy shedding, a large southward retreat of the LC happens, and the LC needs, therefore, a longer period to grow again to a size when it can shed a new eddy. Smaller eddies, on the other hand, trigger a smaller volume loss and, therefore, the LC can grow and shed an additional eddy in a shorter period. Given the small sample size available (with 21 eddies in total), the values provided in Fig. 9 might differ from the real mean, so these numbers should be taken as indicative.

Note that the observed relation applies only to the period that *follows* an eddy of a given size. The opposite relation is not verified; that is, large eddies are not preceded by longer periods between eddy-shedding events. From our data we can infer that, after a small eddy is shed from the LC, another eddy will be shed in a short period of time. However, we cannot expect that a large eddy will be shed from the LC because we observe a large period without eddies being shed. The influence that the size of an eddy has on the time until the next eddy is shed might be important in the understanding of the LC dynamics and to simulate and forecast the LC eddy-shedding events.

b. Loop Current extreme intrusions into the Gulf of Mexico

The LC presented an extreme intrusion into the GoM from 3 to 14 September 2005. During this period the LC was visible up to 27°N and west to 92°W. This extreme intrusion of the LC into the GoM has been rarely seen before. In the 13-yr SSH time series, only four such

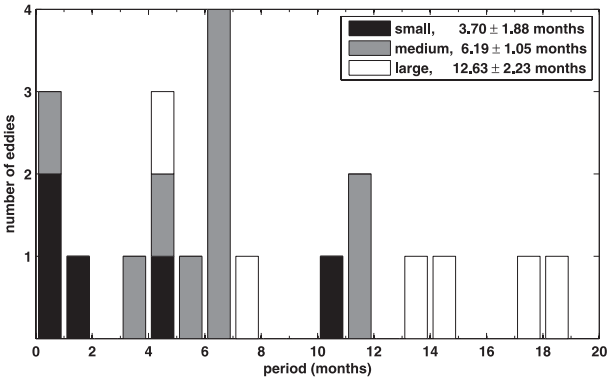

FIG. 9. Number of eddies and relation to the period that followed until the next eddy-shedding event (e.g., four eddies were followed by a period from 6 to 7 months until the next eddy-shedding event). The size of the shed eddies is included with eddies smaller than 150 km considered as small, eddies from 150 to 250 km as medium, and eddies larger than 250 km as large. The mean shedding period observed for each size class is given in the legend, along with the standard error of the mean value (calculated as $\sigma/\sqrt{n}$, with n the number of eddies observed for each size class).

events have been observed. Moreover, one event took place from 23 June to 14 July 1993, whereas the other three occurred within the last four years of this study: 9 January–20 February 2002, 3–14 September 2005, and 7 January–1 February 2006 (see Fig. 10). The duration of these events varies from 2 to 8 weeks. Notice the elongated form of the LC during these events, finer than when the LC presents a normal intrusion into the GoM.

We also measured the frequency of LC large northward intrusions, defined as the LC being north of 27°N, but without the western intrusion of the previous extreme events. The northern limit of 27°N was chosen to be above the mean maximum LC intrusions, estimated as 26.2°N by Leben (2005). There are five periods when the LC extended north of 27°N, as seen in Fig. 10. These events, along with the eddies shed from the LC, are included in Fig. 11. There is an absence of large LC intrusions into the GoM from 1993 to 1999. One possible explanation for this behavior is that the LC has been more stable since 1999, allowing it to grow larger without shedding an eddy. A large intrusion of the LC into the GoM has the direct consequence of providing a conduit for the Mississippi River water to be rapidly advected toward the Florida Keys. Mississippi River water is rich in nutrients and suspended matter (e.g., Hu et al. 2005); therefore, such plumes can cause large ecological perturbations.

Studies involving the transport through the SF and the LC intrusion into the GoM (e.g., Maul and Vukovich 1993) have found no strong evidence of a relationship between these two variables. We looked at the transport through the SF at 27°N (east coast of Florida), presented in section 3, and its relation with the northward intrusions. The cable data are shown in Fig. 11, with a 60-day low-pass filter. The SF transport is generally reported as being stable with a mean transport from 30.5 to 32.2 Sv (Schott et al. 1988; Baringer and Larsen 2001; Hamilton et al. 2005).

During the 13 years of our study, the transport through the SF has a mean value of 32.16 Sv. The four extreme intrusions happen when the SF transport is decreasing, regardless of the total transport (Fig. 11). This relationship suggests that, when the LC is growing, less water may exit through the SF, with the difference in the net transports taken up by compensatory flows in the Yucatan Strait and the Old Bahama/Northwest Providence Channels, thereby keeping the Gulf of Mexico volume nearly constant. This is consistent with the countercurrent structure found on the eastern side of the Yucatan by Sheinbaum et al. (2002). We do not, however, find the same relationship for the other less extreme LC intrusions. Three out of the five events happen when the transport is increasing or at a local maximum. Another event happens during a minimum in transport, and for the last one there are no transport data. The relation between the transport through the SF and the extent of the LC intrusion into the GoM suggests that the conditions for an extreme LC intrusion are different from the mechanism influencing the usual northern LC intrusion, at least in what involves the transport variability.

There are fewer measurements for the YC transport than for the SF. Sheinbaum et al. (2002) found a mean transport through the YC of 23.8 ± 1 Sv from mid-1999 to mid-2000. During this period we observed one large LC intrusion into the GoM (from 21 July to 22 September 1999; see Table 1). Sheinbaum et al. (2002) measured an anomalously low and decreasing transport through the Yucatan Channel during this interval (see their Fig. 4). It is possible that a decreasing inflow allows the LC to grow farther to the north, with the decrease in transport inducing a more stable current less prone to an eddy-shedding event. This, however, must be confirmed by repeated observations.

We also looked at the influence of the LC intrusions in the periods between eddy-shedding events of Table 1. The total number of eddies does not appear to be influenced by the presence of large LC intrusions. There were 9 eddies detached from the LC from October 1992 to June 1999, when there were no large LC intrusions, and 12 eddies from July 1999 to February 2006. The presence of these large intrusions does, however, have an impact on the eddy-shedding frequency: while the

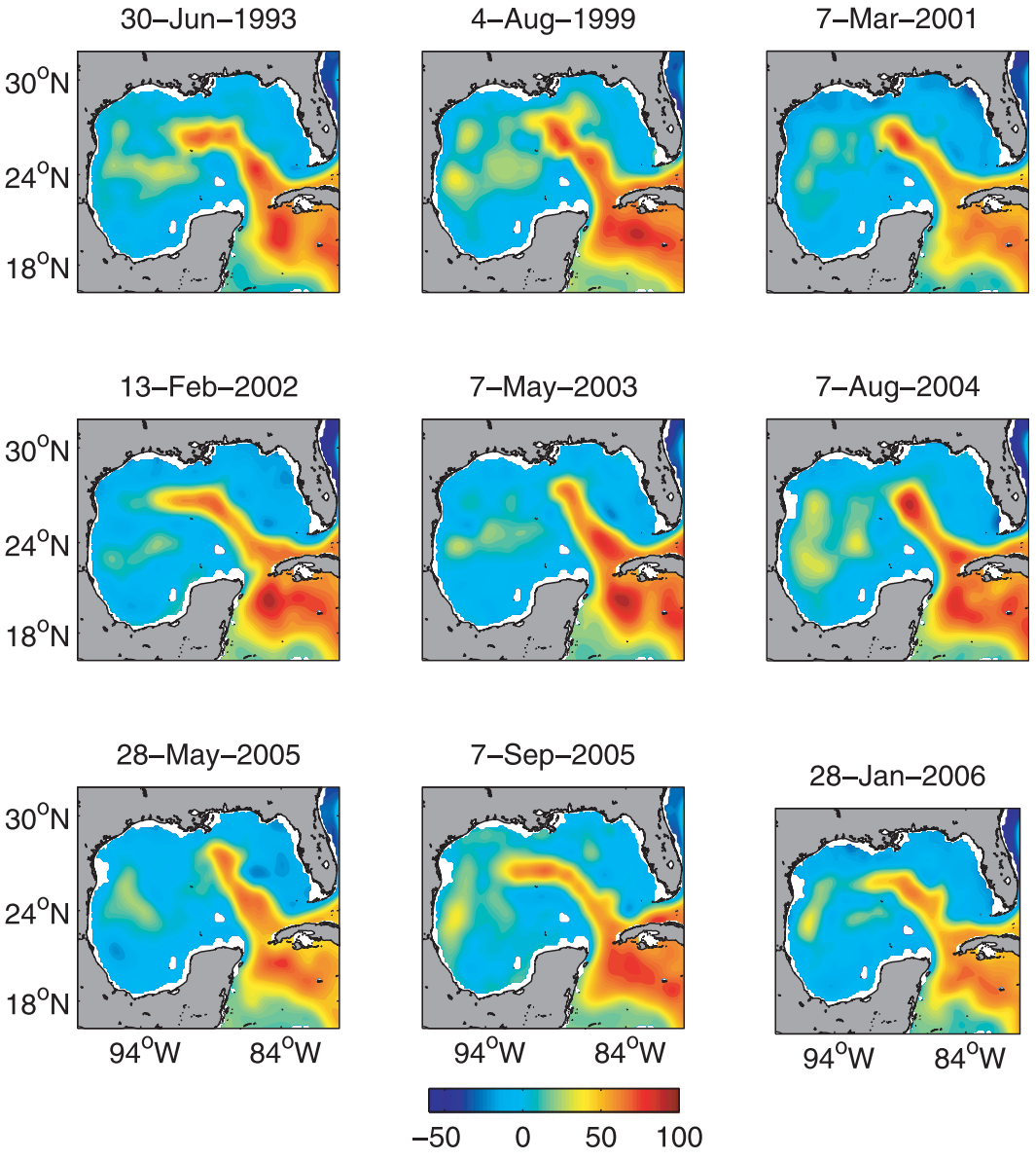

FIG. 10. Large northern LC intrusions into the GoM, including the four extreme intrusions where the LC was seen up to 92°W.

LC is growing to a large GoM intrusion, there is a lack of eddy-shedding events, resulting in an increased eddy-shedding period. These large intrusions shed relatively small eddies (~100 km) because the LC is narrow and unstable near its edge. The shedding of a small eddy results in a limited LC southward retreat. The LC can then rapidly grow and shed another eddy, decreasing the eddy-shedding period. For that reason the periods between eddy shedding are more regular from 1992 to 1999 (when there were no large northern intrusions) than from 1999 to the present, but overall the number of shed eddies does not vary significantly (Fig. 11).

Our corollary finding is a relation between the LC size and the size of the shed eddies. Provided in Fig. 12 is an estimate of these two parameters for the eddies of Table 1, along with the least squares best fit line and its equation. Rather than measuring the LC after it retreats southward, we provide here the distance from Cuba to the point of rupture between the LC and the eddy. Smaller eddies are shed at larger distances measured from the base of the LC. After the shedding of a small eddy, the LC retreats less to the south. As mentioned before, this allows the LC to rapidly grow again and shed another eddy. The spread from the regression line

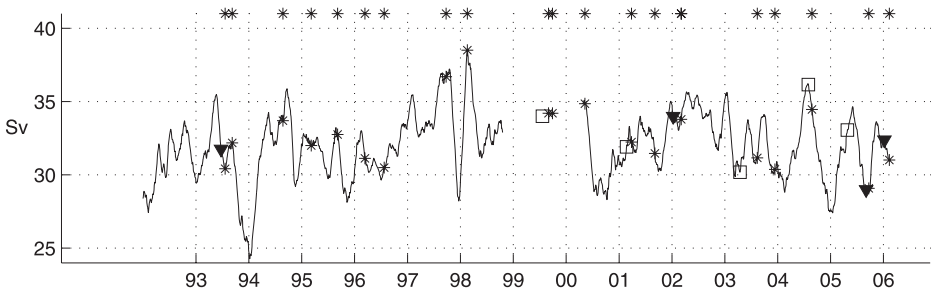

FIG. 11. Transport through the Florida Straits (60-day filtered). Also included are the north LC intrusions (squares) and the extreme LC intrusions (triangles). The moments when an eddy sheds from the LC are marked by an asterisk (for clarity, the asterisks are also included at the top of the figure). Labels mark 1 Jan of each year.

has a mean residual of 135 km and is larger for small eddies. This indicates a larger variability in the distance at which small eddies are shed. The correlation between the eddy size and the length of the LC is strong ($r = 0.66$, significant at the 99% level). The relation found in Fig. 12 is stronger when only eddies larger than 200 km are considered (the correlation is 0.74 in that case). The reason that larger eddies are always shed at small distances from Cuba is found in the shape of the LC: a compact LC is able to shed large eddies, but the intrusion of a compact LC into the GoM is not very large (all eddies larger than 200 km are shed at distances less than 450 km from Cuba). An elongated LC with a large intrusion into the GoM, as seen in Fig. 10, is able to shed only small eddies near its unstable edge, so no large eddies are shed when large LC intrusions into the GoM occur, as pointed earlier in this work. This study complements an analysis made by Leben (2005), where the relation between the time between eddy-shedding events and the southward retreat of the LC is studied. As seen from Fig. 12, the LC size (or southward retreat) is a consequence of the size of the shed eddy, and these two factors affect the subsequent separation period. Figure 9 also showed the relation between the size of a shed eddy (which is related to the LC southward retreat) and the time until the next eddy shedding.

5. Conclusions

The mesoscale circulation of the Caribbean Sea and the Gulf of Mexico (GoM) was examined using a 13-yr sea surface height (SSH) dataset. Geostrophic currents were derived from the SSH. Along with the basin-scale circulation, we focused on the propagation characteristics of Caribbean eddies. We also studied the LC eddy-shedding events as well as a series of extreme LC intrusions in the GoM.

SSH variations at annual to interannual time scales were examined by a complex EOF analysis. Whereas for the Caribbean Sea the annual cycle consists mainly of a steric variation (i.e., the response of the surface layers to the heating and cooling atmospheric heat fluxes), interannual variations, occurring over an approximate 4-yr cycle, consist of variations of the north–south slope across the Caribbean Current, therefore affecting its geostrophic transport. The 4-yr cycle appears to be related to changes in the intensity of the westward wind and the wind stress curl over the Caribbean Sea (with a correlation of -0.6) and to the El Niño–Southern Oscillation index (ENSO, with a correlation of 0.7). This 4-yr cycle accounts for up to 12% of the total transport of the Caribbean Current, and it might have a large impact on the time variability of the current downstream of the Caribbean Sea. For example, the transport found by Sheinbaum et al. (2002) in the Yucatan Channel (YC) was significantly smaller (23.8 Sv) than what is routinely measured in the Florida Straits (32.2 Sv). However, the YC measurements were taken in 1999–2000 when the transport in the Caribbean Sea showed a minimum of the 4-yr cycle (see Fig. 7). Although the interannual variability identified here may have affected the transport through the YC, a longer time series of transport through this channel is necessary to verify this hypothesis.

In addition to the 4-yr cycle in the Caribbean Sea, anomalous conditions were observed in winter 2003. The termination of the 2002 El Niño, the anomalous position of the ITCZ, and a wetter-than-average atmosphere may have contributed to a positive sea level anomaly in the Caribbean Sea during the 2003 winter, and this may have resulted in a greater heat transport by the Caribbean Current.

The Caribbean Current regularly exhibits eddylike features, the propagation of which was examined in the Venezuela–Colombia Basin using the idealized, two-layer Phillips model. These features form and propagate as baroclinic instabilities under the combined influence of vertical shear and the β effect. This result highlights

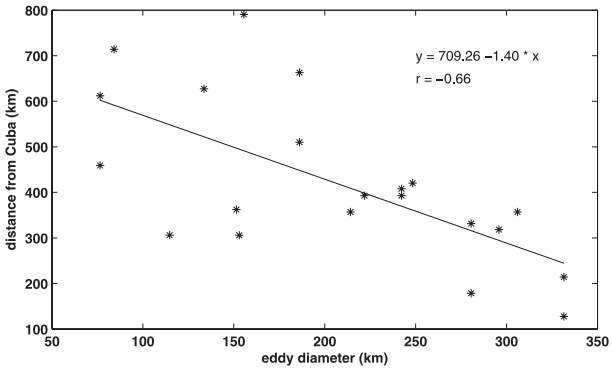

FIG. 12. Relation between the size of an eddy and the distance from Cuba to the point of rupture between the LC and the eddy.

the importance of both the stabilizing effect of the planetary vorticity gradient and the destabilizing effect of shear in the propagation of Caribbean Sea meanders and eddies.

Focusing on the GoM and the LC, we found that the frequency of large LC intrusions into the GoM has recently increased. Three events, extending as far as 92°W, took place from 2002 to 2006, versus only one such event previously (in 1993). Relative to the transport through the SF, all of these events took place during a local decreasing transport trend. Whether such extreme LC intrusions are part of a longer cycle or just isolated events remains a topic for future study based on longer time series.

The entire process of LC intrusion and eddy-shedding remains a research topic, including the conditions under which an eddy sheds from the LC. A relationship was identified between the distance of the LC intrusion into the GoM and the size of a shed eddy. The interval between eddy shedding was found to depend on the LC retreat caused by the eddy size. Large LC intrusions shed small eddies, followed by rapid LC growth and additional eddy shedding. With a ''normal'' LC intrusion, larger eddies are shed, and the interval between eddy shedding is longer. When examining the eddy-shedding phase, 12 out of 21 eddies separated between July and September, suggesting a seasonality in these events.

From these results it is clear that much work remains to fully understand the dynamics of the Caribbean Sea and the GoM. Continuous measurement of the sea surface height anomaly, and the examination of derived variables, provides an evolving dataset that should lead to improved understanding of these ''Intra-Americas Seas.''

Acknowledgments. This research has been funded by Office of Naval Research Grants N00014-02-1-0972 and N00014-05-1-0483 and the National Science Foundation Grant OCE-0326268. The altimeter SLA data were produced by Ssalto/Duacs and distributed by Aviso, with support from CNES. The Florida Current cable data are easily accessible (available online at http://www.aoml.noaa.gov/) and are funded by the NOAA Office of Climate Observations. NRL is acknowledged for providing the data from the HYCOM model (available online at http://hycom.rsmas.miami.edu/dataserver/). ICOADS winds were obtained online (available online at http://icoads.noaa.gov/). The National Fund for Scientific Research (F.N.R.S.), Belgium is acknowledged for funding the postdoctoral position of the two first authors. We wish to acknowledge two anonymous reviewers and the editor M. A. Spall for their useful comments.

APPENDIX

Radon Transform

The Radon transform provides the projection of the Hovmöller diagram (containing the SSH variations in the Caribbean Sea with time) at a specified range of angles varying from 0 to π. The angle zero is situated along the x axis of Fig. 3, that is, along the spatial dimension of the diagram, and it increases to π counterclockwise. The SSH data are projected at each angle, and the summation of the projection is performed. The propagation speed (u) is calculated from the angle (θ) that maximizes the squared sum of the projection:

$$u = \frac{\Delta x}{\tan(\theta)\Delta t}, \tag{A1}$$

where Δx and Δt are the spatial and temporal increments of the Hovmöller diagram. To calculate the standard deviation of the estimated propagation speed, we calculated the second derivative of the squared sum of the projection obtained by the radon transform (p):

$$p'' = \frac{p_{i+1} - 2p_i + p_{i-1}}{\Delta\theta^2}. \tag{A2}$$

The second derivative at the angle that maximizes the radon transform (θ_m), normalized by the value of the radon transform at the same angle [$q = p''/p(\theta_m)$], is used to calculate the standard deviation:

$$\sigma = \sqrt{\frac{2}{q(\theta_m)}}. \tag{A3}$$

This gives the standard deviation in radians. The standard deviation in meters per second is then calculated using Eq. (A1).

REFERENCES

Baringer, M. O., and J. C. Larsen, 2001: Sixteen years of Florida Current transport at 27°N. *Geophys. Res. Lett.,* **28,** 3179–3182.

Bretherton, C. S., M. Widmann, V. P. Dymnikov, J. M. Wallace, and I. Bladé, 1999: The effective number of spatial degrees of freedom of a time-varying field. *J. Climate,* **12,** 1990–2009.

Carton, J. A., and Y. Chao, 1999: Caribbean Sea eddies inferred from TOPEX/Poseidon altimetry and a 1/6° Atlantic Ocean model simulation. *J. Geophys. Res.,* **104** (C4), 7743–7752.

Cassou, C., L. Terray, and A. Phillips, 2005: Tropical Atlantic influence on European heat waves. *J. Climate,* **18,** 2805–2811.

Centurioni, L. R., and P. P. Niiler, 2003: On the surface currents of the Caribbean Sea. *Geophys. Res. Lett.,* **30,** 1279, doi:10.1029/2002GL016231.

Challenor, P., P. Cipollini, and D. Cromwell, 2001: Use of the 3D Radon transform to examine the properties of oceanic Rossby waves. *J. Atmos. Oceanic Technol.,* **18,** 1558–1566.

Chassignet, E. P., and Z. D. Garraffo, 2001: Viscosity parameterization and the gulf stream separation. *From Stirring to Mixing in a Stratified Ocean: Proc. 'Aha Huliko'a Hawaiian Winter Workshop*, Honolulu, HI, University of Hawaii at Manoa, 39–43.

——, H. E. Hurlburt, O. M. Smedstad, G. R. Halliwell, P. J. Hogan, A. J. Wallcraft, R. Baraille, and R. Bleck, 2007: The HYCOM (Hybrid Coordinate Ocean Model) data assimilative system. *J. Mar. Syst.,* **65,** 60–83.

Chelton, D. B., R. A. deSzoeke, M. G. Schlax, K. El Naggar, and N. Siwertz, 1998: Geographical variability of the first baroclinic Rossby radius of deformation. *J. Phys. Oceanogr.,* **28,** 433–460.

Dorandeu, J., and P. Y. Le Traon, 1999: Effects of global mean atmospheric pressure variations on mean sea level changes from TOPEX/Poseidon. *J. Atmos. Oceanic Technol.,* **16,** 1279–1283.

Ducet, N., P. Y. Le Traon, and G. Reverdin, 2000: Global high resolution mapping of ocean circulation from the combination of TOPEX/Poseidon and ERS-1/2. *J. Geophys. Res.,* **105** (C8), 19 477–19 498.

Fratantoni, D. M., 2001: North Atlantic surface circulation during the 1990's observed with satellite-tracked drifters. *J. Geophys. Res.,* **106** (C10), 22 067–22 093.

Fratantoni, P. S., T. N. Lee, G. P. Podesta, and F. Muller-Karger, 1998: The influence of Loop Current perturbations on the formation and evolution of Tortugas eddies in the southern Straits of Florida. *J. Geophys. Res.,* **103** (C11), 24 759–24 779.

Fuller, W. A., 1996: *Introduction to Statistical Time Series*. 3rd ed. Wiley, 698 pp.

Goni, G. J., and W. E. Johns, 2001: A census of North Brazil current rings observed from TOPEX/Poseidon altimetry: 1992–1998. *Geophys. Res. Lett.,* **28,** 1–4.

Hamilton, P., G. S. Fargion, and D. C. Biggs, 1999: Loop Current eddy paths in the western Gulf of Mexico. *J. Phys. Oceanogr.,* **29,** 1180–1207.

——, J. C. Larsen, K. D. Leaman, T. N. Lee, and E. Wadell, 2005: Transports through the Straits of Florida. *J. Phys. Oceanogr.,* **35,** 308–322.

Hart, J. E., 1974: On the mixed stability problem for quasi-geostrophic ocean currents. *J. Phys. Oceanogr.,* **4,** 349–356.

Hernández-Guerra, A., and T. M. Joyce, 2000: Water masses and circulation in the surface layers of the Caribbean at 66°W. *Geophys. Res. Lett.,* **27,** 3497–3500.

Hetland, R. D., Y. Hsueh, R. R. Leben, and P. P. Niiler, 1999: A Loop Current-induced jet along the edge of the West Florida Shelf. *Geophys. Res. Lett.,* **26,** 2239–2242.

Hu, C., J. R. Nelson, E. Johns, Z. Chen, R. H. Weisberg, and F. E. Müller-Karger, 2005: Mississippi River water in Florida Straits and in the Gulf Stream off Georgia in summer 2004. *Geophys. Res. Lett.,* **32,** L14606, doi:10.1029/2005GL022942.

Johns, W. E., T. L. Townsend, D. M. Fratantoni, and W. D. Wilson, 2002: On the Atlantic inflow to the Caribbean Sea. *Deep-Sea Res. I,* **49,** 211–243.

Killworth, P. D., 1980: Barotropic and baroclinic instability in rotating stratified fluids. *Dyn. Atmos. Oceans,* **4,** 143–184.

Kontoyiannis, H., 1997: Quasi-geostrophic modeling of mixed instabilities in the Gulf Stream near 73°W. *Dyn. Atmos. Oceans,* **26,** 133–158.

Larnicol, G., P. Y. Le Traon, N. Ayoub, and P. De Mey, 1995: Mean sea level and surface circulation variability of the Mediterranean Sea from 2 years of TOPEX/Poseidon altimetry. *J. Geophys. Res.,* **100** (C12), 25 163–25 177.

Leben, R. R., 2005: Altimeter-derived Loop Current metrics. *Circulation in the Gulf of Mexico: Observations and Models, Geophys. Monogr.,* Vol. 161, Amer. Geophys. Union, 181–201.

——, and G. H. Born, 1993: Tracking Loop Current eddies with satellite altimetry. *Adv. Space Res.,* **13,** 325–333.

Lee, T. N., K. Leaman, E. Williams, T. Berger, and L. Atkinson, 1995: Florida Current meanders and gyre formation in the southern Straits of Florida. *J. Geophys. Res.,* **100** (C5), 8607–8620.

Le Traon, P.-Y., and F. Ogor, 1998: ERS-1/2 orbit improvement using TOPEX/Poseidon: The 2 cm challenge. *J. Geophys. Res.,* **103,** 8045–8057.

——, F. Nadal, and N. Ducet, 1998: An improved mapping method of multisatellite altimeter data. *J. Atmos. Oceanic Technol.,* **15,** 522–534.

Levinson, D. H., and A. M. Waple, 2004: State of the climate in 2003. *Bull. Amer. Meteor. Soc.,* **85,** S1–S72.

Maul, G. A., and F. M. Vukovich, 1993: The relationship between variations in the Gulf of Mexico Loop Current and Straits of Florida volume transport. *J. Phys. Oceanogr.,* **23,** 785–796.

Molinari, R. L., I. Spillane, D. Brooks, D. Atwood, and C. Duckett, 1981: Surface currents in the Caribbean Sea as deduced from Lagrangian observations. *J. Geophys. Res.,* **86,** 6537–6542.

Morrison, J. M., and O. P. Smith, 1990: Geostrophic transport variability along the Aves Ridge in the eastern Caribbean Sea during 1985–1986. *J. Geophys. Res.,* **95** (C1), 699–710.

Murphy, S. J., H. E. Hulburt, and J. J. O'Brien, 1999: The connectivity of eddy variability in the Caribbean Sea, the Gulf of Mexico, and the Atlantic Ocean. *J. Geophys. Res.,* **104** (C1), 1431–1453.

Oey, L.-Y., H.-C. Lee, and W. J. Schmitz Jr., 2003: Effects of winds and Caribbean eddies on the frequency of Loop Current eddy shedding: A numerical model study. *J. Geophys. Res.,* **108,** 3324, doi:10.1029/2002JC001698.

Pedlosky, J., 1979: *Geophysical Fluid Dynamics.* Springer-Verlag, 624 pp.

Phillips, N. A., 1954: Energy transformations and meridional circulations associated with simple baroclinic waves in a two-level, quasi-geostrophic model. *Tellus,* **6,** 273–286.

Pratt, R. W., and G. A. Maul, 2000: Sea surface height variability of the Intra-Americas Sea from TOPEX/Poseidon satellite altimetry: 1992–1995. *Bull. Mar. Sci.,* **67,** 687–708.

Qiao, L., and R. H. Weisberg, 1998: Tropical instability wave energetics: Observations from the Tropical Instability Wave Experiment. *J. Phys. Oceanogr.,* **28,** 354–360.

Richardson, P. L., 2005: Caribbean Current and eddies as observed by surface drifters. *Deep-Sea Res. II,* **52,** 429–463.

Robinson, I. S., 2004: *Measuring the Oceans from Space: The Principles and Methods of Satellite Oceanography*. Springer-Praxis, 669 pp.

Schär, C., P. L. Vidale, D. Lüthi, C. Frei, C. Häberli, M. A. Liniger, and C. Appenzeller, 2004: The role of increasing temperature variability in European summer heatwaves. *Nature,* **427,** 332–336.

Schmitz, W. J. J., 2005: Cyclones and westward propagation in the shedding of anticyclonic rings from the Loop Current. *Circulation in the Gulf of Mexico: Observations and Models, Geophys. Monogr.,* Vol. 161, Amer. Geophys. Union, 241–261.

Schott, F. A., T. N. Lee, and R. Zantopp, 1988: Variability of structure and transport of the Florida Current in the period range of days to seasonal. *J. Phys. Oceanogr.,* **18,** 1209–1230.

Sheinbaum, J., J. Candela, A. Badan, and J. Ochoa, 2002: Flow structure and transport in the Yucatan Channel. *Geophys. Res. Lett.,* **29,** 1040, doi:10.1029/2001GL013990.

Sturges, W., 1994: The frequency of ring separations from the Loop Current. *J. Phys. Oceanogr.,* **24,** 1647–1651.

——, and R. Leben, 2000: Frequency of ring separations from the Loop Current in the Gulf of Mexico: A revised estimate. *J. Phys. Oceanogr.,* **30,** 1814–1819.

Vukovich, F. M., 1995: An updated evaluation of the Loop Current's eddy-shedding frequency. *J. Geophys. Res.,* **100** (C5), 8655–8659.

Walsh, J. J., and Coauthors, 2003: Phytoplankton response to intrusions of slope water on the West Florida Shelf: Models and observations. *J. Geophys. Res.,* **108,** 3190, doi:10.1029/2002JC001406.

Weisberg, R. H., and R. He, 2003: Local and deep-ocean forcing contributions to anomalous water properties of the West Florida Shelf. *J. Geophys. Res.,* **108,** 3184, doi:10.1029/2002JC001407.

Wolter, K., 1987: The Southern Oscillation in surface circulation and climate over the tropical Atlantic, Eastern Pacific, and Indian Oceans as captured by cluster analysis. *J. Climate Appl. Meteor.,* **26,** 540–558.

Worley, S., S. Woodruff, R. Reynolds, S. Lubker, and N. Lott, 2005: ICOADS release 2.1 data and products. *Int. J. Climatol.,* **25,** 823–842.

Zavala-Hidalgo, J., S. L. Morey, and J. J. O'Brien, 2003: Cyclonic eddies northeast of the Campeche Bank from altimetry data. *J. Phys. Oceanogr.,* **33,** 623–629.